JOURNAL OF THERMOPHYSICS AND HEAT TRANSFER
Vol. 9, No. 1, January–March 1995

Influence of Two-Phase Thermocapillary Flow on Liquid Retention in Microscopic Pores

George R. Schmidt*
NASA Marshall Space Flight Center, Huntsville, Alabama 35812
and
Arun Nadarajah,† T. J. Chung,‡ and Gerald R. Karr§
University of Alabama in Huntsville, Huntsville, Alabama 35899

An important feature of screened propellant acquisition devices is the retention capability or maximum maintainable pressure difference across the porous barrier separating the liquid and gas. Previous experiments with liquid hydrogen showed a marked reduction in retention when the tank containing the device was pressurized with hydrogen vapor. These tests, however, did not indicate any appreciable degradation in retention with helium pressurization or direct heating through the screen. The objective of this article is to determine if the thermocapillary convection arising from phase change in the microscopic pores of such screens could cause these disparities in performance. A numerical model of flow in a single pore suggests that the thermocapillary-induced gradient in liquid pressure along the surface can strongly affect surface morphology. In an evaporative environment, this gradient exerts a stabilizing influence on surface curvature, and preserves the momentum balance between the liquid and gas. With condensation, it causes a force imbalance and a destabilizing suction in the middle of the pore that reduces retention. Results also indicate that introducing an inert gas, such as helium, suppresses this retention loss mechanism by lowering thermocapillary circulation and its associated interfacial pressure gradient.

Nomenclature

a_i = Earth-normalized acceleration, $i \equiv$ direction
D = characteristic dimension, pore width
e = accommodation coefficient
F_i = thermocapillary stress force, $i \equiv$ direction
g_0 = Earth acceleration magnitude
k = thermal conductivity
L = latent heat
M_W = molecular weight
n_i = i-direction component of unit vector normal to surface
P = pressure
P_d = dynamic pressure
P_h = hydrostatic pressure
$P^{(v)}$ = vapor pressure at T_0
R_g = universal gas constant
s = contour position
s_i = i-direction component of unit vector tangent to surface
T = temperature
T_0 = vapor temperature
t = time
V_i = velocity, $i \equiv$ direction
x_i = Cartesian coordinates
$y^{(s)}$ = meniscus surface x_2 position
$y_0^{(s)}$ = meniscus x_2-coordinate centerline
α = contour angle of liquid surface
β = expansion coefficient
Γ = surface area
γ = surface tension
ΔP_b = bubble point pressure
$|\Delta T|$ = subcooling/superheating temperature limit
ζ = thermal diffusivity
Θ_i = modified stress force, $i \equiv$ direction
κ = surface curvature
μ = dynamic viscosity
ν = kinematic viscosity
ρ = density
τ_{ij} = viscous stress tensor, $i \equiv$ direction, $j \equiv$ surface
Ψ = stream function
ω = contact angle

Subscripts

i = first-order tensor index
$,i$ = $\partial/\partial x_i$
ij = second-order tensor index
$,ij$ = $\partial^2/\partial x_i \partial x_j$

Dimensionless Parameters

Bi = Biot number, $1/RsE$
Bo = bond number, $\rho g_0 D^2/\gamma$
Ca = capillary number, $\rho \nu^2/\gamma D$
Cr = crispation number, $|\partial\gamma/\partial T||\Delta T|/\gamma$
E = evaporation number, $k|\Delta T|/\rho \nu L$
f_ρ = ratio of liquid to vapor density
Gr = Grashoff number, $D^3 g_0 \beta |\Delta T|/\nu^2$
Ma = Marangoni number, $|\partial\gamma/\partial T|D|\Delta T|/\rho\nu\zeta$
Pr = Prandtl number, ν/ζ
Rs = interfacial resistance, $f_\rho \nu T_0^{3/2}(2\pi R_g/M_W)^{1/2}/eDL|\Delta T|$
Vr = recoil parameter, $Ca(f_\rho - 1)/Rs^2$

Presented as Paper 94-0836 at the AIAA 32nd Aerospace Sciences Meeting, Reno, NV, Jan. 10–13, 1994; received Feb. 28, 1994; revision received July 21, 1994; accepted for publication July 22, 1994. Copyright © 1994 by the American Institute of Aeronautics and Astronautics, Inc. No copyright is asserted in the United States under Title 17, U.S. Code. The U.S. Government has a royalty-free license to exercise all rights under the copyright claimed herein for Governmental purposes. All other rights are reserved by the copyright owner.

*Chief, Advanced Propulsion Branch, Propulsion Laboratory. Member AIAA.

†Assistant Professor, Department of Chemical Engineering. Member AIAA.

‡Professor, Department of Mechanical Engineering. Member AIAA.

§Professor and Department Chairman, Department of Mechanical Engineering. Member AIAA.

Introduction

An important aspect of fluid transfer in low gravity is the acquisition of gas-free liquid from storage tanks. In such an environment, the orientation of the bulk liquid surface is unpredictable and dictated almost wholly by the competition between acceleration and surface tension forces. Passive devices that exploit surface tension to hold the fluid in a desired location are often used to acquire liquid and foster its expulsion.[1,2] These liquid acquisition devices (LADs) have been used on spacecraft for some time, primarily to control nonvolatile propellants and liquids. Their operational simplicity has also made them appealing options for future applications with cryogenic propellants and liquids.

Numerous LAD concepts have been proposed and used over the years. A schematic of one common design, a partial control-type device, is shown in Fig. 1. Most LADs rely on fine mesh screens that allow liquid to pass into a channel or trap while inhibiting the flow of gas. This unique feature arises from the meniscus formed by surface tension between the mesh and liquid. As long as liquid adheres to the screen wires, gas is kept out of the channel, and a pressure difference can be sustained to effect flow through the device. The maximum pressure difference that can be maintained between the gas and liquid is the retention capability, and it is an important characteristic of the porous surface. Also known as the bubble point pressure ΔP_b, retention is usually expressed as the force balance on a circular pore, i.e., $\Delta P_b = 4\gamma \cos \omega / D$, where D is the hydraulic diameter and characteristic dimension of the screen. Because the wire weaves of most screens are too complex to characterize analytically, ΔP_b must be determined from experiments. The hydraulic diameters of commercial screens range considerably, but are available with dimensions as small as 1–10 μm.

The bubble point of nonvolatile liquids is relatively immune to the minute departures in thermodynamic equilibrium caused by venting, pressurization, or conduction through the screen structure. With cryogens and saturated fluids, however, several experiments since the early 1970s have shown retention to be sensitive to the pressurant environment. Among the earliest of these was Burge and Blackmon,[3] who tested the retention capabilities of fine mesh screen samples in liquid hydrogen (LH2) while subjected to warm hydrogen pressurant. They found that heating the vapor by only 5–10 K above the bulk liquid temperature caused premature breakdown (i.e., retention loss), and lowered the effective ΔP_b. A later screen sample experiment, which evaporated the vapor away from the surface, did not incur any noticeable reduction in retention. However, a third test of a screen basket pressurized with hydrogen vapor encountered retention loss at temperatures of 40 K. Blackmon[4] later tested a vertically oriented screen channel with LH2 and found that warm pressurant, regardless of gas type, resulted in premature breakdown. The reduction in retention was as much as 70% of the design bubble point pressure with hydrogen vapor, but was only 20% with helium. Tests with colder hydrogen pressurant, close to its saturation temperature, did not yield any premature retention loss.

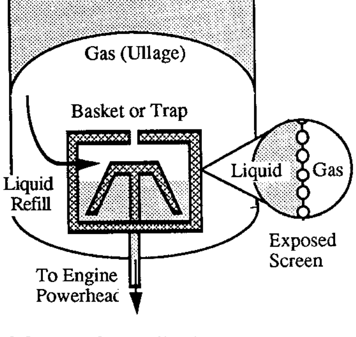

Fig. 1 Partial control-type liquid acquisition device (LAD).

Cady[5] later measured the bubble points of various screen samples subjected to different calibrated heating rates, and found that the maximum reduction in bubble point was less than 15%. In spite of test conditions being deliberately established to superheat the liquid with respect to the pressurant, wicking through the screen and evaporation at the surface adequately absorbed the heat. Paynter and Page[6] and Warren[7,8] conducted LH2 expulsion tests in a total communication-type LAD, and failed to observe premature breakdown during periods of continuous outflow, regardless of pressurant type or temperature. In tests with intermittent flow, however, retention loss occurred repeatedly with warm hydrogen, but not with warm helium. Bennett[9] also conducted experiments with a start basket in LH2. In all hydrogen pressurant tests, a vapor at approximately 90 K was injected into a test dewar, and the screen failed before the liquid level was lowered to the bottom of the basket. On average, the hydrostatic head at the point of failure was 50% of the screen bubble point. With helium pressurant the liquid level could always be lowered below the basket, and retention was demonstrated for periods of up to several hours.

The most recent investigation of LH2 retention was performed by Meserole and Jones,[10] who measured the breakdown pressure of a semicircular screened channel with different pressurant types, temperatures, and degrees of liquid stagnation. With helium, no measurable variation in performance was observed, and retention loss in every test was close to the predicted screen bubble point. With hydrogen vapor, however, retention exhibited a strong sensitivity to pressurant temperature. Cool vapor at approximately saturation temperature yielded a retention capability close to predictions. With a warm vapor, the bubble point was significantly reduced, and temperatures as low as 15–20 K above saturation caused sharp reductions in retention.

In general, experiments over the last 20 yr have indicated a reduction in LH2 retention when the porous structure was subcooled with respect to the vapor. Based on the results in Refs. 3–10, Meserole and Jones proposed that evaporative cooling was responsible for the strong tolerance to heated vapor with small screen samples, whereas condensation of warm vapor was the cause for reduced retention in pressurized environments. This conclusion, however, does not constitute a complete explanation, since it fails to address how condensation lowers the effective bubble point. The objective of this study is to identify the mechanism leading to retention loss and explain why it arises when the LAD is subcooled with respect to the vapor. We begin by supposing that the cause is related to the convection arising from thermodynamic nonequilibrium between the liquid and pressurant. The most likely convection modes with the pore sizes considered here are evaporation, condensation, and thermocapillarity. The problem is then to determine if these modes could lead to the retention failures observed in previous experiments.

Model Formulation

Physical Model

One feature that distinguishes this problem from the traditional approach of evaluating pore retention is the departure from thermodynamic equilibrium between the pore structure, liquid, and pressurant gas. It is therefore necessary to consider the various types of nonequilibrium conditions imposed in the aforementioned experiments. We classify these as 1) pressurization with heated vapor,[3,4,6-10] 2) evaporation with an overhead heater,[3,5] 3) evaporation with an overhead heater followed by recirculation over a screen surface,[3] 4) evaporation via conductive heating of a screen,[5] and 5) pressurization with heated helium.[4,6-8,10]

These states generally represent either a superheating or subcooling of the liquid and screen with respect to a saturated vapor. In case 1, which is most susceptible to retention failure, vapor is introduced at a higher pressure and temperature than the saturated liquid in the LAD. Upon pressurization, the liquid becomes subcooled. Regardless of whether the vapor is saturated or superheated, the situation near the meniscus is likely one of a saturated vapor in contact with a subcooled liquid. In cases 2 and 3, vapor is obtained through evaporation, and liquid at the surface becomes superheated with respect to the surrounding vapor. In case 2, the pressurant is not actively recirculated over the screen and no significant retention loss is observed. In case 3, however, recirculation takes place, and retention failures are more numerous. In case 4, liquid is evaporated by heating through the screen wires. Because the entire wire structure is heated, the region of superheat extends all around the pore. Like case 2, there is no significant drop in retention. In case 5, heated helium is introduced at a higher pressure and temperature, similar to the state in case 1. Here, however, the presence of helium near the surface retards evaporation and condensation, and there is no significant reduction in bubble point pressure.

Another unique feature of this problem is the complex geometry of LAD screens. The problem domain can be simplified considerably by assuming that 1) retention failure represents a rupturing of the liquid surface at its point of maximum curvature, and 2) the convection responsible for retention loss is independent of bulk flow within the LAD interior. As described in Ref. 11, these assumptions allow us to apply the simple geometry depicted in Fig. 2, which consists of a square channel partially filled with a Boussinesq liquid.

Although the geometry is similar to that of float-zone problems[12–14] and investigations of thermocapillary convection in wetting liquids[15,16] (see Ref. 11 for a more extensive list of references), there are several differences that make this problem unique. Apart from impermeable left and right side walls, the lower boundary opens to a large reservoir to enable balancing of liquid flow through the cavity and modeling of a capillary structure. The upper surface is represented by a curved meniscus, which is symmetric about the pore centerline and bounded by an inert vapor. The shape of the surface is defined by the height above the base $y^{(s)}$ and is a function of x_1. This study considers a pore dimensional range in which intermolecular attraction between the liquid and solid is modeled best via a fixed acute contact angle ω rather than a corrected surface or body force.[17] The largest dimension at which detailed intermolecular effects become apparent is $\sim 10^{-2}$ μm, which is considerably less than the hydraulic diameters of typical LAD screens.

Another unique aspect is the temperature boundary conditions. Previous studies examining the influence of surface morphology and contact angle[15,16] have maintained the side walls at different temperatures while keeping the upper and lower surfaces adiabatic. In this problem, the side walls and lower boundary are maintained at the same temperature relative to the saturated vapor. The difference between the boundary and vapor temperature ΔT is positive for superheating, and negative for subcooling. Liquid convection is driven by a Robin-type boundary condition along the meniscus that accounts for heat transfer either to or from the liquid.

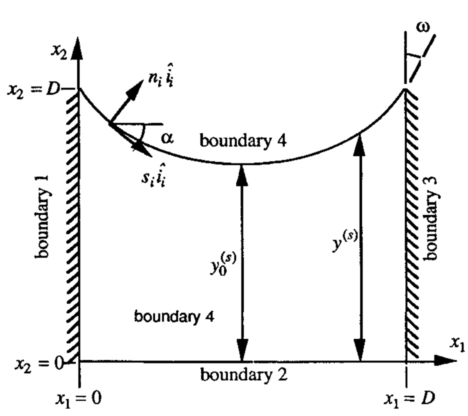

Fig. 2 Problem domain.

Mathematical Model

The dependent variables describing this problem, i.e., V_i, P, T, and $y^{(s)}$, are solved via the Navier-Stokes system of equations, the imposed conditions on boundaries 1, 2, and 3, and the jump conditions across boundary 4. Using the same approach as Burelbach et al.,[17] we apply viscous scales to all variables and nondimensionalize temperature according to the maximum difference in the cavity. The resulting governing equations for continuity, momentum, temperature, and surface curvature are

$$V_{i,i} = 0 \tag{1}$$

$$\frac{\partial V_i}{\partial t} + V_j V_{i,j} + P_{d,i} - \tau_{ij,j} - Gra_i T = 0 \tag{2}$$

$$\frac{\partial T}{\partial t} + V_j T_{,j} - \frac{1}{Pr} T_{,jj} = 0 \tag{3}$$

$$\kappa = \frac{Boy^{(s)} - Ca[P_d - P^{(v)}] + VrT^2 + 2CaV_{i,j}n_jn_i}{1 - Cr\bar{T}} \tag{4}$$

P_d is viewed as the departure from hydrostatic pressure arising from flow effects, where $P = P_h + P_d$. The scaling of T is intentional so that the vapor always assumes a dimensionless temperature of 0. Note that with superheating the side wall temperature is fixed at $T = 1$, whereas with subcooling, it is held at $T = -1$. All fluid properties are scaled according to the minimum domain temperature, which is fixed at the saturated vapor temperature with superheating or the side wall temperature with subcooling.

Like the other boundary 4 equations, Eq. (4) is derived by applying the one-sided approximation in which we assume vanishing ratios between vapor and liquid viscosities and thermal conductivities. The terms $Boy_0^{(s)}$, $Ca[P_d - P^{(v)}]$, VrT^2, $2CaV_{i,j}n_jn_i$, and $(1 - Cr\bar{T})^{-1}$ represent the normal force contributions of hydrostatic pressure, dynamic pressure, vapor recoil, viscous stress, and surface tension thermal variation, respectively. $\bar{T}$ is a corrected scaled temperature whose value depends on the maximum and minimum temperature in the cavity. For superheating $\bar{T} = T$, whereas for subcooling $\bar{T} = T + 1$.

An important parameter in the recoil term of Eq. (4) is Rs, which defines the degree of nonequilibrium (i.e., the difference in state between the liquid and vapor) that can be maintained per unit mass undergoing phase change at a volatile interface. It is derived by applying the perfect gas law and equilibrium thermodynamic assumptions to the Hertz-Knudsen equation.[18] The factor e in Rs is used to reflect the resistance to mass transfer caused by foreign molecules in the vapor or condensed phase. Its value can range from 0 for the nonvolatile case to 1 for a volatile surface free of contaminants.

For boundaries 1 and 3, we have $V_1 = 0$, $V_2 = 0$, and $T = \pm 1$, which reflect impermeability, no-slip, and isothermal temperature, respectively. For boundary 2, we assume the same temperature as the side walls and hold $T = \pm 1$. There are several ways to handle velocity along boundary 2. We followed the simplest approach and assumed uniform parallel flow, where $V_1 = 0$, and V_2 is obtained by balancing the mass flows across boundaries 2 and 4, i.e.,

$$V_2 = \frac{1}{\Gamma_2} \int_{\Gamma_4} \frac{T}{Rs} \, d\Gamma_4 \tag{5}$$

Equation (5) treats boundary 4 as stationary and is consistent with our numerical approach of solving the meniscus outside the steady-state flowfield solution.

The boundary equations for surface 4 consist of Neumann, Dirichlet, and Robin-type conditions for V_1, V_2, and T, respectively. For V_1 we have the one-sided tangential stress balance:

$$\tau_{ij}n_j = -(Ma/Pr)T_{,i} \tag{6}$$

The normal gradients of V_1 and V_2 are interdependent and mutually satisfied by applying the Neumann condition to either velocity component. By applying Eq. (6) to V_1, an expression for V_2 falls out of the condition for local mass flux, i.e.,

$$V_2 = (1/n_2)[(T/Rs) - V_1n_1] \tag{7}$$

For temperature, we apply the one-sided approximation in balancing heat flux into and out of the surface. We ignore kinetic energy transport, which is negligible for very small length scales. This yields the following general relationship:

$$T_{,i}n_i = -BiT \tag{8}$$

Bi relates the rate of latent heat transfer to heat conduction. It is inversely proportional to Rs and E, the latter of which represents the ratio between viscous and evaporation/condensation time scales (i.e., D^2/ν and $\rho D^2L/(k|\Delta T|)$, respectively).[17] The parameter E is indicative of the rate of phase change relative to momentum diffusion in the cavity, whereas Rs dictates the rate at which vaporized liquid leaves or condensed vapor deposits onto the surface. Thus, Rs can either augment or restrict the influence of phase change on pore heat transfer. For example, increasing the rate of mass transport (i.e., lowering Rs) reduces the rate limiting effects of phase change and its influence on interfacial temperature.

In addition to the flow and thermal variable equations, we also have two conditions that must be satisfied to solve Eq. (4). One is the pinning condition, where $y^{(s)} = 1$ at $x_1 = 0$ and 1. The other is the contact angle constraint at the side walls, which in terms of Cartesian coordinates is $|\mathrm{d}y^{(s)}/\mathrm{d}x_1| = \tan(\pi/2 - \omega)$ at $x_1 = 0$ and 1. Recognizing that $Ca = f(Cr, Pr, Ma)$ and $Vr = f(Ca, f_\rho, Rs)$, we find that Pr, Gr, Ma, Rs, f_ρ, Cr, Bo, and Bi represent a consistent set of independent parameters.

Numerical Model

Since a detailed description of the numerical model is given in Ref. 11, we will only summarize its key features here. The finite element method was selected mainly because of its strength in handling unstructured grid domains and free boundaries. Although it is possible to structure a numerical solution so that the surface is determined simultaneously with V_i, P_d, and T, this approach is memory intensive and requires manipulation of an extremely large sparse coefficient matrix.

An alternative approach, which was implemented in Refs. 13 and 14, relaxes the normal stress boundary condition and calculates surface position $y^{(s)}$ in an iteration loop outside the steady-state flowfield solution. This is justified since Eq. (4) is independent of the rate of surface deflection. In this "trial method," the meniscus solution is the outermost iteration in a five-loop flowfield solution procedure. The first loop determines a velocity field that satisfies Eq. (2) based on an estimated pressure distribution. The second loop (i.e., SIMPLER algorithm[19]) adjusts the velocity and pressure field via the results of correction equations formulated from continuity and momentum. Once convergence is established for V_i and P_d, the third loop computes the temperature field. In the fourth loop, the time step is advanced to steady state, and temporal convergence is checked. The criterion is that the average temperature vary no more than 0.01% from its value at the previous time step.

An important aspect of the model is the solution of surface geometry. The problem of accommodating small contact angles is handled by transforming Eq. (4) into an integrable difference equation, noting that $\kappa = \partial\alpha/\partial s$, and treating α and surface position s as dependent and independent variables, respectively.[20,21] The resulting expression is

$$\frac{\partial\alpha}{\partial s} = \frac{\sum - Ca\Delta P_d + Vr\Delta(T^2) + 2Ca\Delta(V_{i,j})n_jn_i + Bo\int_0^s \sin\alpha\,\mathrm{d}s}{1 - Cr\bar{T}} \tag{9}$$

where

$$\sum = Boy_0^{(s)} + Ca[P^{(v)} - P_{d0}] + \frac{(f_\rho - 1)}{Rs^2}T_0^2 + 2V_{0i,j}n_jn_i \tag{10}$$

Between the surface nodes where flowfield data is available, T, V_i, and P_d values are interpolated using the same order as their element level variance. We have expressed Eq. (9) in a form where Σ corresponds to the curvature at the meniscus centerline. Consequently, the curvature at other points along the surface is a function of Σ, and the change in pressure, temperature, and velocity relative to the centerline values, i.e., $\Delta P_d = P_d - P_{d0}$, $\Delta(T^2) = T^2 - T_0^2$, and $\Delta(V_{i,j}) = V_{i,j} - V_{0i,j}$.

The entire surface extending from $x_1 = 0$ to 1 is solved by applying the shooting method to each half of the meniscus. The objective is to determine a Σ that yields the specified ω at the side walls. At $x_1 = 0.5$, we set $\alpha = 0$, assume a value of Σ, and calculate α_i at successive steps along the contour until $x_1 = 0$ or 1. If the final contact angle estimate $\omega_i = \pi/2 - \alpha_i$ fails to match, within a specified tolerance, the desired value of ω, Σ is adjusted, and the contour integration is repeated. The new estimate of Σ is obtained using a simple bisection algorithm, which accommodates large positive and negative Σ.

Basic Flowfield Behavior

Investigating the flow and temperature field about a fixed circular meniscus is useful for understanding how Ma, Rs, Bi, and ω mutually influence the convective terms contributing to surface curvature in Eq. (4). Evaluation of such a domain was performed in Ref. 11 at parameter values corresponding to 1 μm $< D <$ 10^2 μm, with superheating/subcooling levels between 10^{-1} and 1 K. Recognizing that buoyancy and hydrostatic pressure can be ignored in this size range (i.e., Gr and $Bo \to 0$), the four major findings were 1) increasing convective heat transfer relative to conduction (i.e., $Bi \to \infty$) yields a higher thermal gradient and total thermocapillary force on the surface, 2) reducing contact angle also increases this force, 3) increasing the total thermocapillary force raises circulation in each half-cavity (i.e., left and right sides of problem domain in Fig. 2) and promotes large interfacial pressure gradients near the side walls, and 4) relative to the meniscus centerline, these gradients are positive for subcooling and negative for superheating.

The first two findings are illustrated by examining the basic state, where heat transfer between the pore boundaries occurs solely by conduction. To examine this regime, we set $V_i = 0$ and solve the steady-state diffusion equation for temperature $T_{,jj} = 0$, while applying Eq. (8). The temperature distribution is a function of Bi and the geometry of the upper boundary, which for a circular meniscus depends exclusively on contact angle. Although fluid convection and stress are ignored, the surface temperature distribution associated with the basic state yields a reference $\partial T/\partial s$, from which a normalized thermocapillary force, based only on the nonlinear influence of Bi and ω, can be calculated, i.e.,

$$\Theta_m = -Bi \int_\Gamma T \frac{g_k s_k}{g_j n_j} s_m \, \mathrm{d}\Gamma \tag{11}$$

The parameter Θ_m is the nonlinear contribution to the total thermocapillary force F_m in the x_m direction, where F_m = $(Ma/Pr)\Theta_m$. The unit vector $\hat{g}$ $(= g_i \hat{\imath}_i)$ is parallel to the surface temperature gradient ∇T $(= T_{,i} \hat{\imath}_i)$, and $g_k s_k/g_j n_j$ is the ratio between the tangential and normal components of interfacial heat flux. Important to this problem is the manner in which Θ_m varies with ω. In the x_1 direction, the magnitude of Θ_1 exerted on each half-cavity surface Θ_1'' tends to increase as $\omega \rightarrow 90$ deg, because the interfacial temperature gradient becomes larger to accommodate the smaller surface area for heat transfer. The total contribution of Θ_1 equals zero, however, because the thermocapillary stress and half-cavity force exhibit mirror-symmetry about the centerline. The only force component that remains when we consider the entire surface is the x_2 component or Θ_2. The relationship between Θ_2 for the basic state (i.e., Θ_{2b}) and Bi and ω is shown in Fig. 3. Reducing contact angle generally increases Θ_{2b}, whereas flattening the surface causes Θ_{2b} to vanish. The sensitivity of Θ_2 to the contact angle also becomes greater as $Bi \rightarrow \infty$, due to the increasing temperature gradient in the side wall region, where $|s_2|$ is high.

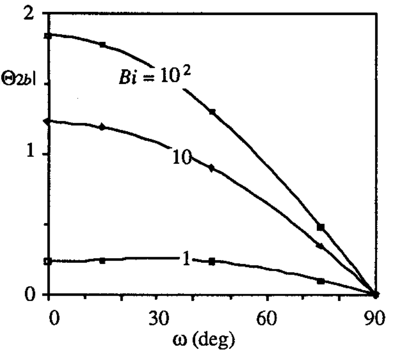

Fig. 3 x_2-component of normalized thermocapillary force vs contact angle. Normalized stress calculated from basic state temperature distribution.

The increase in thermocapillary force with lower contact angles and higher Bi has implications for flow within the pore. To illustrate this, we examined the regime of pure thermocapillary flow at contact angles of 75, 45, and 15 deg. Superheated and subcooled side wall conditions are applied assuming volatility for heat transfer (Bi = 10), but nonvolatility for mass transfer ($Rs \rightarrow \infty$). A low value of Ma = 10^2 is selected to limit convection within the pore and deviation from the basic state temperature distribution. Steady-state solutions for the six cases are shown in Fig. 4, which portrays the half-cavity values of stream function and temperature. This rep-

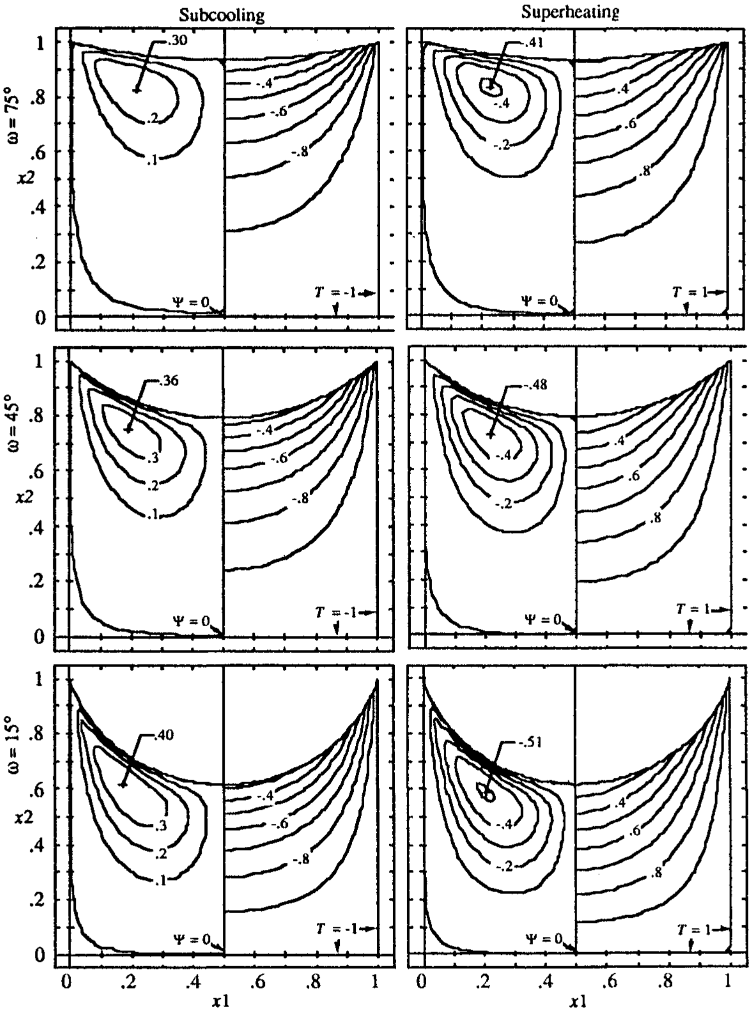

Fig. 4 Sensitivity of stream function and temperature to contact angle. Pure thermocapillary flow with Ma = 10^2 and Bi = 10.

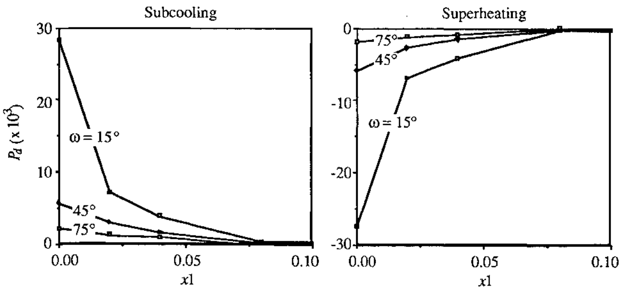

Fig. 5 Interfacial pressure values adjacent to left side wall. Pure thermocapillary flow with $Ma = 10^2$ and $Bi = 10$.

resentation is permissible since all variables exhibit mirror-symmetry about the pore centerline.

For both heating modes, the thermocapillary stress establishes twin counter-rotating vortices on either side of the cavity. With subcooling, the surface traction towards the side walls establishes counterclockwise and clockwise circulations in the left and right half-cavities, respectively. With superheating, the traction points towards the pore centerline, and the sense of cell circulation is opposite.

The most apparent trend in Fig. 4 is the increase in circulation with smaller contact angles, which coincides with the basic state behavior observed for Θ_2. At $\omega = 75$ deg, the surface is relatively flat and most of the applied traction accelerates liquid in the x_1 direction. The momentum of this flow, however, is diminished at the surface by opposing fluid motion from the other side of the cavity. This attenuation of x_1 direction momentum is reflected by the canceling out of Θ_1'' contributions in the calculation of total thermocapillary force. With smaller ω (i.e., 45 deg), a larger portion of the surface traction is applied in the x_2 direction. That is, Θ_2 becomes larger with smaller ω. The x_2 component of momentum is only partially offset by viscous losses along the centerline and stationary boundaries. Consequently, its contribution to circulation grows with increasing traction in the x_2 direction. This is confirmed by the flowfield for $\omega = 15$ deg, which exhibits the strongest circulation of any case.

An important consequence of thermocapillary flow with small contact angles is the large dynamic pressure gradients it produces in the contact region. This effect is illustrated in Fig. 5, which shows the numerical pressure values at the four surface nodes adjacent to the left side wall. The data indicate that dynamic pressure increases dramatically as $\omega \rightarrow 0$, and that the dynamic pressure gradient tends to vanish at large contact angles. In fact, with a contact angle of 15 deg, the pressure can be an order of magnitude higher than the value for a flat surface. The magnitude of the pressure gradient depends on the circulation, whereas its sign is due to the direction of thermocapillary stress. From a physical standpoint, pressure behaves as a force applied at the corner that balances changes in fluid momentum, thermocapillary stress, and friction. Because the momentum change is very sensitive to restrictions in flow area, the pressure gradient is a strong function of contact angle.

Retention Failure Modes

The retention capability of a screen pore is ensured as long as the normal jump momentum balance along the meniscus is maintained. Loss of retention occurs when a force imbalance develops between the gas and liquid. For a static nonvolatile fluid, retention is preserved by keeping the gas/liquid pressure difference below the design bubble point. With a volatile liquid, the condition holds only if a steady-state solution exists that simultaneously satisfies the equations for velocity, pressure, temperature, and surface curvature. To study the influence of convection on retention, we examine coupled solutions of the flowfield and meniscus at parameter values corresponding to the thermodynamic conditions imposed in previous tests.

The normal jump balance, represented by the expression for curvature in Eq. (4), contains five terms that could contribute to a force imbalance. In Ref. 11, the first-order influence of these terms was evaluated using the steady-state flowfield data for fixed geometry pores. The results showed that, for parameter values corresponding to characteristic dimensions of 1–10 μm, and superheat/subcooling levels of 10^{-1} to 1 K, the influence of surface tension variation, viscous stress, and hydrostatic pressure on surface curvature is negligible. Only the terms associated with dynamic pressure and vapor recoil appear to be important.

Within the context of the one-sided model, variation in thermodynamic equilibrium is reflected by the values of Rs and Bi, where $Vr \propto Rs^{-2}$. All other parameters, except contact angle, are fixed at values representative of the dimensional and thermal limits noted above, namely $Ma = 10^2$, $Cr = 10^{-1}$, and $Ca = 10^{-3}$. Instead of considering a zero or very low contact angle, which would properly model hydrogen physical characteristics, we fix ω at 45 deg. It was very difficult to obtain solutions for subcooling at $\omega = 15$ deg, let alone ~0 deg, due to the extremely large interline pressure gradients. By employing a higher ω, the pressure gradient is reduced, and the surface is less sensitive to variations in P_d. Assuming a pure liquid and vapor, we set $Rs = 1$ and $Bi = 10$. The correspondingly low value of recoil parameter (i.e., $Vr \approx 1$ with $f_\rho = 10^3$) suggests that the surface is dictated by dynamic pressure and unaffected by recoil.

The steady-state solutions for this combination of parameters are shown in Fig. 6. Note that the static isothermal solution (SIS) for the $\omega = 45$-deg surface in Fig. 4 has been superimposed on the plots to better illustrate deformation. With subcooling, the solution diverges, and we are unable to obtain convergence between the flowfield and surface. Figure 6 actually represents the steady-state solution after the 16th surface iteration. With subsequent iterations, the depression near the centerline grows until the surface becomes multivalued (i.e., folds over itself) at $x_1 \approx 0.1$ and 0.9. It appears that P_d is strongly influenced by the contour and growing depression after each flowfield solution. During the first few iterations, the meniscus assumes an inflection to accommodate the negative contribution of P_d in Eq. (9). The flat surface around this inflection extends the high pressure into the center, which drives the depression even lower. The depression around the centerline serves to increase Θ_2, and promotes circulation. Thus, the deformation associated with subcooling has the same stress-related effect on P_d as reducing contact angle.

With superheating, a stable steady-state solution was obtained after only eight surface iterations. As the solution converges, the meniscus flattens and decreases in area due to the pressure drop towards the side wall. This tends to reduce the half-cavity circulation by lowering Θ_2 and models the effect of increasing contact angle. It also serves to reduce the side wall pressure gradient and ensures stable numerical conver-

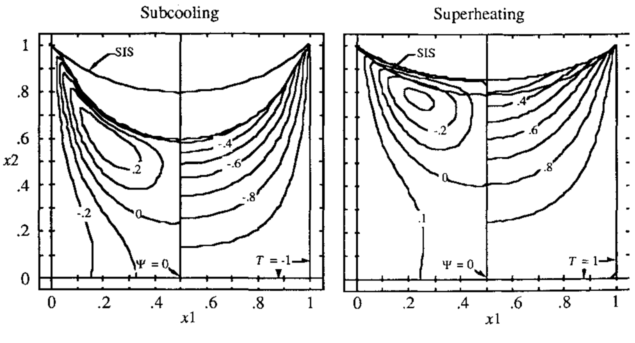

Fig. 6 Steady-state stream function and temperature fields with $Ma = 10^2$, $Rs = 1$, $Bi = 10$, and $Cr = 10^{-1}$.

gence. As long as the surface retains a positive curvature, superheated thermocapillary flow should promote mechanical equilibrium along the surface.

The interfacial pressure arising from thermocapillarity appears to exert a destabilizing influence on subcooled surfaces and is the likely cause for retention loss. Pressurization with a warm vapor subcools liquid on the LAD surface, and through thermocapillary stress establishes a suction that pulls the meniscus down in the middle of the pore. The results also explain the difference in behavior observed with screens heated via conduction and those subjected to heated pressurant. Heating through solid contact models the situation of a superheated pore. This establishes a surface flow towards the centerline and a suction in the vicinity of the side walls, which, unlike subcooling, promotes mechanical equilibrium and a more robust meniscus.

To examine the influence of an inert pressurant, we must account for the relationship between *Bi* and the level of equilibrium between the vapor and liquid (i.e., *Rs*). The degree of vapor/liquid equilibrium is embodied by *e*, which is lowered by the presence of foreign molecules in either the condensed or vapor phase. The previous setting of *e* to unity was appropriate for modeling kinetics of a pure liquid in contact with its own vapor. An inert gas, however, should suppress this interaction, and from the standpoint of the one-sided model, decrease *e*.

The reduction in *e* caused by raising helium concentration is modeled by increasing *Rs* and lowering *Bi*, while holding *E*, which depends solely on liquid properties and $|\Delta T|$, constant. This is illustrated in Figs. 6–8. In these cases, *E* is held at 10^{-1}, while *Rs* is increased incrementally from 1 to 2 to 10, and *Bi* is lowered from 10 to 5 to 1. As noted before, the subcooling regime in Fig. 6 is insolvable due to the destabilizing effect of dynamic pressure, while the superheating regime is stable.

At the next increment of *Rs* (=2) in Fig. 7, we obtain a stable solution for subcooling, and the surface exhibits only a slight depression around the centerline. Although no inflection is evident, the surface does become relatively straight near the side walls. The surface temperature gradient is also lower than the case in Fig. 6, and causes a drop in circulation intensity and thermocapillary convection. With superheating, we encounter the same general behavior as Fig. 6. However, the increase in *Rs* and reduction in side wall pressure gradient decreases the effect of recoil and dynamic pressure causing the surface to drop closer to the SIS curve. With *Rs* = 10 (Fig. 8), the circulation drops dramatically for both heating modes, and the surface in both cases converges to a shape that is very close to the static isothermal geometry.

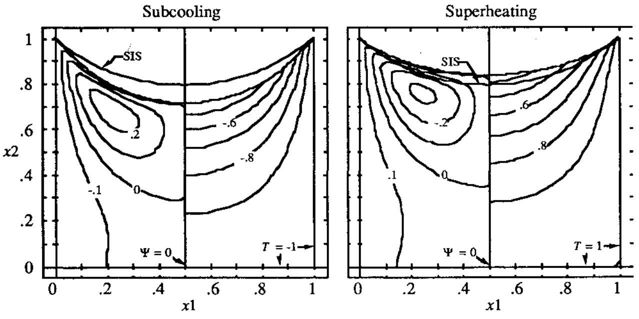

Fig. 7 Steady-state stream function and temperature fields with $Ma = 10^2$, $Rs = 2$, $Bi = 5$, and $Cr = 10^{-1}$.

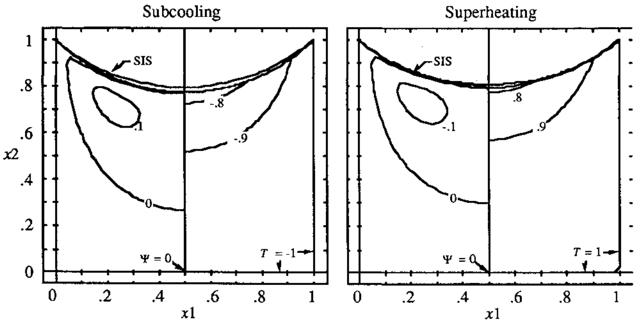

Fig. 8 Steady-state stream function and temperature fields with $Ma = 10^2$, $Rs = 10$, $Bi = 1$, and $Cr = 10^{-1}$.

Reduction in accommodation coefficient appears to restrict both half-cavity circulation and the deformation associated with pressure and vapor recoil. This is especially true for subcooling, which, based on a simple decrease in *e*, can transition from an unstable solution to one that is completely well-behaved. Although we have only sketchily studied this phenomenon, it provides a plausible explanation for the resistance to retention failure exhibited in LAD tests with gaseous helium. Regardless of whether the gas presents a subcooled or superheated environment, the transition into a more convection-limited interfacial temperature distribution suppresses the pressure gradients associated with thermocapillary flow.

Conclusions

The steady-state solution of a pore with a deformable surface has been examined. Using parameter values approximately representative of liquid hydrogen exposed to its own vapor, we evaluated the response of the surface to several heating modes, including pressurization with heated vapor, screen conduction, and pressurization with heated helium. The results support the original hypothesis of retention loss being caused by convection within the screen pores of liquid acquisition devices. The reduced performance with pressurized heated hydrogen vapor is caused by the thermocapillary flow arising from condensation-induced temperature gradients along the liquid surface. This flow establishes an interfacial pressure distribution that deforms the center of the surface into the liquid. The situation is physically unstable for highly wetting liquids, since the deformation serves to increase the total thermocapillary force and pressure gradient even further. The outcome of such deformation is an expansion of the meniscus into the liquid and eventual detachment from the screen wires.

The resistance to retention loss with heated helium pressurant is due to evaporation at the surface, which establishes a thermocapillary flow structure opposite to that with hydrogen pressurization. Instead of depressing the meniscus, the pressure gradient tends to raise the surface in the center of the pore. This situation is inherently stable because the deformation serves to reduce the thermocapillary force, circulation, and interfacial pressure gradient. As long as wicking through the screen accommodates evaporative losses, pressurization with heated helium promotes mechanical equilibrium of the surface and improves retention.

The immunity to retention loss with direct screen heating is attributed to the same stabilizing behavior. Since the vapor surrounding the screen is not pressurized with respect to the liquid, the pore menisci are superheated relative to the vapor. The same thermocapillary flow pattern encountered with helium pressurization develops, and, provided the wicking rate is adequate, the screen exhibits nominal or improved retention performance.

References

[1] Blatt, M. H., Stark, J. A., and Siden, L. E., "Low Gravity Propellant Control Using Capillary Devices in Large Cryogenic Vehicles—Design Handbook," General Dynamics Corp. Convair Div., GDC-DDB70-006, San Diego, CA, Aug. 1970.

[2] Dodge, F. T., "Fluid Management in Low Gravity," *Low-Gravity Fluid Dynamics and Transport Phenomena*, edited by J. N. Koster and A. R. Seebass, Vol. 130, Progress in Astronautics and Aeronautics, AIAA, Washington, DC, 1990, pp. 1–18.

[3] Burge, G. W., and Blackmon, J. B., "Study and Design of Cryogenic Propellant Acquisition Systems—Vol. II," McDonnell Douglas Astronautics, MDC G5038, Huntington Beach, CA, Dec. 1973.

[4] Blackmon, J. B., "Design, Fabrication, Assembly and Test of a Liquid Hydrogen Acquisition Subsystem," McDonnell Douglas Astronautics, MDC G5360, Huntington Beach, CA, May 1974.

[5] Cady, E. C., "Design and Evaluation of Thermodynamic Vent/Screen Baffle Cryogenic Storage System," McDonnell Douglas Astronautics, MDC G5360, Huntington Beach, CA, June 1975.

[6] Paynter, H. L., and Page, G. R., "Acquisition/Expulsion Orbital Propulsion System Study—Vol. II: Cryogenic Design," NASA CR-134154, Oct. 1973.

[7] Warren, R. P., "Acquisition System Environmental Effects Study," Martin Marietta, MCR-75-21, Denver, CO, May 1975.

[8] Warren, R. P., "Measurements of Capillary System Degradation," AIAA Paper 75-1197, Sept. 1975.

[9] Bennett, F. O., "Design and Demonstrate the Performance of Cryogenic Components Representative of Space Vehicles—Start Basket Liquid Acquisition Device Performance Analysis," General Dynamics, Space Systems Division, GDSS-CRAD-87-004, San Diego, CA, Feb. 1987.

[10] Meserole, J. S., and Jones, O. S., "Pressurant Effects on Cryogenic Liquid Acquisition Devices," *Journal of Spacecraft and Rockets*, Vol. 30, No. 2, 1993, pp. 236–243.

[11] Schmidt, G. R., "Thermocapillary Flow with Evaporation and Condensation and Its Effect on Liquid Retention in Low-g Fluid Acquisition Devices," Ph.D. Dissertation, Univ. of Alabama in Huntsville, Huntsville, AL, 1993; also NASA TP-3463, Feb. 1994.

[12] Ostrach, S., "Fluid Mechanics in Crystal Growth—The 1982 Freeman Scholar Lecture," *Journal of Fluids Engineering*, Vol. 105, No. 1, 1983, pp. 5–20.

[13] Cuvelier, C., and Driessen, J. M., "Thermocapillary Free Boundaries in Crystal Growth," *Journal of Fluid Mechanics*, Vol. 169, Aug. 1986, pp. 1–26.

[14] Hyer, J., Jankowski, D., and Neitzel, G., "Thermocapillary Convection in a Model Float Zone," *Journal of Thermophysics and Heat Transfer*, Vol. 5, No. 4, 1991, pp. 577–582.

[15] Keller, J. R., and Bergman, T. L., "Thermocapillary Cavity Convection in Wetting and Nonwetting Liquids," *Numerical Heat Transfer Part A*, Vol. 18, 1990, pp. 33–49.

[16] Kamotani, Y., and Platt, J., "Effect of Free Surface Shape on Combined Thermocapillary and Natural Convection," *Journal of Thermophysics and Heat Transfer*, Vol. 6, No. 4, 1992, pp. 721–726.

[17] Burelbach, J. P., Bankoff, S. G., and Davis, S. H., "Nonlinear Stability of Evaporating/Condensing Liquid Films," *Journal of Fluid Mechanics*, Vol. 195, Oct. 1988, pp. 463–494.

[18] Kennard, E., *Kinetic Theory of Gases*, 1st ed., McGraw-Hill, New York, 1938.

[19] Patankar, S. V., *Numerical Heat Transfer and Fluid Flow*, Hemisphere, Washington, DC, 1980.

[20] Concus, P., "Static Menisci in a Vertical Right Circular Cylinder," *Journal of Fluid Mechanics*, Vol. 34, No. 3, 1968, pp. 481–495.

[21] Geiger, F., "Hydrostatics of a Fluid in a Cylindrical Tank at Low Bond Numbers," Brown Engineering Research Labs., TN R-207, Huntsville, AL, July 1966.